

Discovery of the Hidden State in Ionic Models Using a Domain-Specific Recurrent Neural Network

Shahriar Iravanian *

Abstract

Ionic models, the set of ordinary differential equations (ODEs) describing the time evolution of the state of excitable cells, are the cornerstone of modeling in neuro- and cardiac electrophysiology. Modern ionic models can have tens of state variables and hundreds of tunable parameters. Fitting ionic models to experimental data, which usually covers only a limited subset of state variables, remains a challenging problem. In this paper, we describe a recurrent neural network architecture designed specifically to encode ionic models. The core of the model is a Gating Neural Network (GNN) layer, capturing the dynamics of classic (Hodgkin-Huxley) gating variables. The network is trained in two steps: first, it learns the theoretical model coded in a set of ODEs, and second, it is retrained on experimental data. The retrained network is interpretable, such that its results can be incorporated back into the model ODEs. We tested the GNN networks using simulated ventricular action potential signals and showed that it could deduce physiologically-feasible alterations of ionic currents. Such domain-specific neural networks can be employed in the exploratory phase of data assimilation before further fine-tuning using standard optimization techniques.

1. Introduction

Ionic models, the set of ordinary differential equations (ODEs) describing the time evolution of the state of excitable cells, are the mainstay of cellular and tissue modeling in neuro- and cardiac electrophysiology. The first ionic model was the two-variable Hodgkin-Huxley model of the squid giant axon [10]. This model was successful in explaining the generation and propagation of action potentials. Since then, thousands of models have been proposed for various types of excitable cells in different species [5, 6].

The majority of ionic models have retained the general structure of the Hodgkin-Huxley model while adding a large degree of complexity. For example, the

*Division of Cardiology, Section of Electrophysiology, Emory University Hospital, Atlanta, GA, USA (shahriar.iravanian@emoryhealthcare.org)

O’Hara-Rudy human ventricular model has 41 state variables in its most basic form [15]. The large number of parameters raises major concerns regarding over-fitting, validity, and lack of predictive power. The general process to develop a new model is to separate and characterize different ionic currents individually using patch clamping techniques in isolated cells and then combine all these separate pieces into a coherent model based on the behavior of the whole cell. One major obstacle to the latter step is that only one or two of the state variables are actually detectable in tissue experiments, while other variables remain *hidden*. The primary *observable* state variable in cardiac and neuronal ionic models is the transmembrane potential, which can be measured using either micro-electrodes or optical mapping techniques after staining the tissue with voltage-sensitive fluorescent dyes [8]. The second observable in some experimental setup is the concentration of intracellular calcium that can be measured using optical mapping and calcium-sensitive dyes.

Our main problem can be cast as how to deduce and optimize the dynamics of excitable cells when most of the state variables are hidden. Of course, this is not a unique situation and occurs repeatedly in system identification field. Over the years, many different optimization and probabilistic methods, under the general moniker of data assimilation, have been adopted to solve hidden-state identification in ionic models [1, 4, 11, 13, 16, 21].

In the last few years, scientific machine learning has emerged as a powerful alternative to the traditional methodology in the study of dynamical systems [19]. It tries to combine machine learning methods, such as deep neural networks, with prior domain knowledge encoded in ODEs and partial differential equations (PDEs). Scientific machine learning is especially useful in situations when we have an imperfect or poorly defined physical model but a large amount of experimental data, as is the case of system identification for ionic models.

According to the universal approximation theorem, it is not surprising that neural networks can be used to describe dynamical systems. However, the black-box nature of neural networks is a significant drawback, as we need an *interpretable* and *explainable* representation of the model. The keys to a successful application of scientific machine learning are, first, to be able to encode our prior knowledge (generally in the form of a system of ODEs) into the model, and second, to be able to interpret the outputs of the model.

In this paper, our goal is to develop a machine learning architecture (a domain-specific recurrent neural network) to solve the hidden-variable identification in ionic models and to help with optimizing model parameters. Specifically, we like to find the optimized version of an ionic model for a given time-series of observables. The main motivation for this study was the challenges we faced trying to apply established ionic models to experimental data. For example, in one case, we had a large amount of optical mapping data from guinea pig hearts before and after the infusion of QT prolonging medications. Our initial plan was to verify the experimental data by using a standard guinea pig ventricular model [14]. However, we noted that baseline simulated data did not match perfectly to

the experimental baseline data. Therefore, we had to modify the model to fit the observed baseline data before searching the large parameter space to find a solution to the effects of the medication. In summary, we were faced with a non-perfect and inexact ionic model, which, at the same time, could not be ignored, as it encoded the bulk of our prior knowledge of the system of interest.

2. Methods

2.1 Overview

We start by describing the motivating example (see above) in a more formal language. Let \mathcal{M} be an ionic model and let \mathbf{X} and \mathbf{Y} be two datasets composed of the observables of \mathcal{M} recorded before and after some interventions (e.g., application of a membrane-active drug). Our goal is to find \mathcal{M}' , a modification of \mathcal{M} , that explains the effects of the intervention. In theory, \mathcal{M} should reproduce \mathbf{X} . In practice, \mathcal{M} is imperfect, and its output deviates from \mathbf{X} . Our solution is to

1. Train a neural network \mathcal{N} to learn \mathcal{M} .
2. Retrain \mathcal{N} on the control dataset \mathbf{X} to obtain \mathcal{N}_X .
3. Retrain \mathcal{N} on the treatment dataset \mathbf{Y} to obtain \mathcal{N}_Y .
4. Modify \mathcal{M} based on \mathcal{N}_X and \mathcal{N}_Y to obtain \mathcal{M}_X and \mathcal{M}_Y (assuming the neural networks are interpretable).
5. Read the effects of the intervention by comparing \mathcal{M}_X and \mathcal{M}_Y .

In section 2.2, we provide a general overview of the ionic models (\mathcal{M}). Sections 2.3 and 2.4 are dedicated to describing our neural network architecture and the core of its interpretability, the GNN (Gating Neural Network) layer. Training and retraining methods are discussed in sections 2.5 and 2.6. Finally, in section 2.7, we show how to convert neural networks back to neural-ODEs, which are amenable to integration using standard ODE solvers. The main difficulty lies in the last step, as neural networks are usually considered to be black-boxes. As we will explain, our networks are designed with a focus on the interpretability of their internals.

2.2 Generic Ionic Models

In this section, we set up the preliminary definitions and describe the generic structure of the ionic models before explaining our machine learning model in the subsequent sections.

Let $\mathbf{u} = \{u_i\}$ be the state vector, composed of k state variables. For most ionic models, the state variables, u_i , are of three main types: V_m , which is the transmembrane potential and is the main observable, one or more intracellular ion concentrations, and multiple gating variables.

The system is defined as an ODE, $\mathbf{u}' = \mathbf{f}(\mathbf{u}, t)$, where prime denotes time derivation. The dynamics of the gating variables follows the generic Hodgkin-

Huxley formulation. Each gating variable has a value in the range 0 to 1 and evolves according to (say, for a variable m),

$$m' = \alpha(V_m)(1 - m) - \beta(V_m)m, \quad (2.2.1)$$

where α and β are the reactivation and deactivation rates, respectively. The rates are dependent on V_m and, in some models, on other ionic concentrations, but never on the gating variables. We will use this fact in the next section to derive a simplified recurrent network layer. From hereon, we drop the explicit dependence on V_m to reduce clutter. Eq. 2.2.1 is usually written as,

$$m' = \frac{m_\infty - m}{\tau_m}, \quad (2.2.2)$$

for

$$m_\infty = \frac{\alpha}{\alpha + \beta}, \quad (2.2.3)$$

and

$$\tau_m = \frac{1}{\alpha + \beta}, \quad (2.2.4)$$

where m_∞ and τ are the steady-state value and the time-constant of m and are functions of V_m .

The dynamics of V_m is described as

$$V_m' = \frac{1}{C_m} \left(\sum_j I_j(\mathbf{u}) + I_{\text{stim}}(t) \right), \quad (2.2.5)$$

where I_j s are various transmembrane currents, which can depend on any of the state variables but not directly on t , C_m is a constant quantifying the membrane capacitance, and I_{stim} is the time-varying external stimulation current.

The fast sodium current (here for the ten Tusscher ventricular model, see below) is a good example of the form of the equations describing ionic currents,

$$I_{\text{Na}} = g_{\text{Na}} m^3 h j (V_m - E_{\text{Na}}(\text{Na}_i, \text{Na}_o)), \quad (2.2.6)$$

where m , h , and j are gating variables. In Eq. 2.2.6, g_{Na} is a model parameter and the sodium reversal potential (E_{Na}) is a function of the intracellular and extracellular sodium concentrations.

In addition to V_m and the gating variables, \mathbf{u} also includes various intracellular concentrations. The general ODE for a typical concentration (say c) is

$$c' = f_c(c, I_c), \quad (2.2.7)$$

where I_c is the current corresponding to c . In contrast to classic gating variables, I_c , and hence c' , may depend on gating variables.

In summary, an ionic model is composed of a state variable \mathbf{u} , the initial values, $\mathbf{u}(0)$, and a set of ODEs similar to Eqs. 2.2.2, 2.2.5, and 2.2.7. In many cardiac applications, a one-, two- or three-dimensional Laplacian of V_m is added to the right side of Eq. 2.2.5 to form a system of PDEs. In this paper, we limit ourselves to the study of the ODE form of the ionic models.

A common feature of the ionic models, especially the cardiac ones, is the presence of two or more time scales. Usually, V_m and some gating variables, like m and h , are fast; whereas, ionic concentrations and some other gating variables are slow (tens to hundreds of milliseconds). Specially, m_∞ and τ in Eq. 2.2.2 can be considered constant for the duration of one time step ($\Delta t \lesssim 1$ ms). Therefore, we can explicitly integrate Eq. 2.2.2 to obtain

$$m(t + \Delta t) = m_\infty + (m(t) - m_\infty) e^{-\Delta t/\tau}. \quad (2.2.8)$$

This trick is called the Rush-Larsen method and forms the core of our recurrent network (see section 2.4) [20].

2.3 General Network Architecture

The key ingredient of scientific machine learning is the fusion of deep learning techniques with traditional scientific knowledge, usually encoded as systems of ODEs and PDEs. Here, we limit our discussion to initial-value ODEs,

$$\mathbf{u}' = \mathbf{f}(\mathbf{u}, t; \theta), \quad (\text{Eq. 2.3.1})$$

where \mathbf{u} is the state vector, t is time, θ represents model parameters, and the initial condition, $\mathbf{u}(0)$ is known. A general framework to mix ODEs with machine learning is provided by the concept of universal ordinary differential equations (UODE) [17]:

$$\mathbf{u}' = \mathbf{f}(\mathbf{u}, t, U_{\theta'}(\mathbf{u}, t); \theta). \quad (\text{Eq. 2.3.2})$$

The machine learning part is provided by $U_{\theta'}(u, t)$ representing a universal approximator – a neural network, a random forest, a Chebychev expansion, or any other suitable approximator. In a UODE, $U_{\theta'}(u, t)$ replaces part or the

entirety of the ODE derivative function. For the rest of the paper, we assume that $U_{\theta'}$ is a neural network, therefore

$$\mathbf{u}' = \mathbf{f}(\mathbf{u}, t, \text{NN}_{\theta'}(\mathbf{u}, t); \theta). \quad (\text{Eq. 2.3.3})$$

One of the main challenges of building a UODE model is at the interface of the neural network, NN, and the ODE when NN require access to the ODE estimated error during training. One possible solution is to use ODE sensitivity analysis (using adjoint equations) to provide an estimate of the error that then back-propagates into NN. Another challenge in applying UODE methodology to solving ionic models is that most of the variables in the state vector remain unobservable. In Eqs. 2.3.1-2.3.3, it is implicitly assumed that \mathbf{u} is observable. As mentioned above, in electrophysiology (and many other fields), only a limited subset of the state variables is observable, and the rest is hidden. We address this problem by using recurrent neural networks (RNN). A typical feed-forward neural network is stateless; however, we can make it stateful by adding recurrent layers. The resulting RNN is better equipped in representing dynamical maps that flows. Therefore, we modify our ODE system to a map,

$$\mathbf{v}(t + \Delta t) = \mathbf{f}(\mathbf{v}, t, \text{RNN}_{\theta', \mathbf{h}}(\mathbf{v}, t); \theta), \quad (\text{Eq. 2.3.4})$$

where $\mathbf{v} \in \mathbf{u}$ is the set of observables and \mathbf{h} stands for the hidden state. In essence, the neural network becomes an ODE integrator. We can make another simplification by absorbing the entirety of the ODE system into the recurrent network by setting \mathbf{f} to the identity function, and $\theta' = \theta$ to get

$$\mathbf{v}(t + \Delta t) = \text{RNN}_{\theta, \mathbf{h}}(\mathbf{v}, t). \quad (\text{Eq. 2.3.5})$$

Eq. 2.3.5 forms the basis of our neural network. The most commonly used recurrent layer is the long short-term memory or LSTM layer [7, 9]. Although LSTM has been very successful in general applications, it lacks easy interpretability. Therefore, we simplified and modified the LSTM into the GNN (described in section 2.4), a recurrent layer that is specifically optimized for Hodgkin-Huxley style gating variables. However, not all the state variables in ion models are classic gating variables. We incorporate an LSTM layer in our network to handle these variables, accepting the trade-off of losing interpretability for them.

Figure 1 depicts the schematic of our network. The network is composed of two sub-networks: \mathcal{N}_1 , which is ϕ_1 plus a GNN layer, and \mathcal{N}_2 , which is formed from ϕ_2 , an LSTM layer, and ϕ_3 . \mathcal{N}_1 handles the classic gating variables, and therefore uses a GNN layer. \mathcal{N}_2 is responsible for other state variables (non-classic gates, concentrations, and V_m) with the help of its LSTM layer. The other layers (ϕ_1, ϕ_2, ϕ_3) are standard dense and fully-connected one or two-layer deep networks.

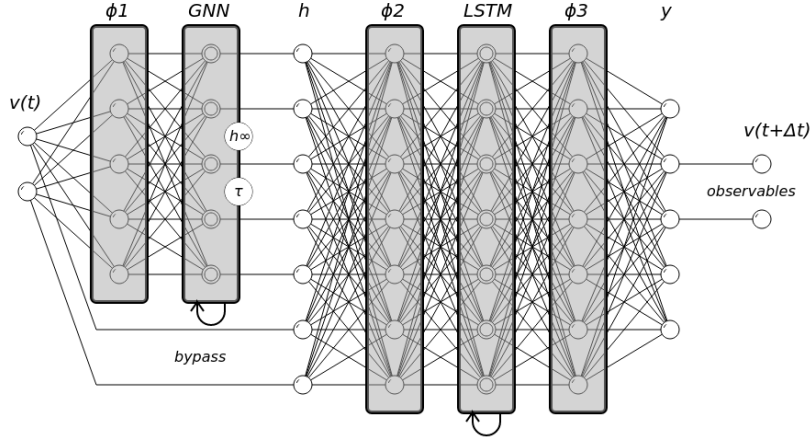


Figure 1: The general schematic of our neural network architecture. The network is composed of two sub-networks: \mathcal{N}_1 , formed by $\phi 1$ (two fully-connected dense layers) and GNN (a domain-specific recurrent layer), and \mathcal{N}_2 , formed by $\phi 2$, $\phi 3$, and a recurrent layer (LSTM).

The entire network transforms the observables at time t , i.e., $\mathbf{v}(t)$, to the observables at $t + \Delta t$. However, the output of \mathcal{N}_1 , which corresponds to the gating variables, is exposed and is used for training. Note that the input, $\mathbf{v}(t)$, is fed to both \mathcal{N}_1 and, via a bypass, to \mathcal{N}_2 .

2.4 Gating Neural Network (GNN)

The GNN is a recurrent layer designed to *integrate* Hodgkin-Huxley gating state variables based on Eq. 2.2.8. The goal is the ease of training and interpretability. Each GNN layer stores a state vector, $\mathbf{h}(t)$, which generally corresponds to the gating variables of \mathbf{u} .

At each time step, $\mathbf{h}(t)$ is updated. We need the steady-state value, $\mathbf{h}_\infty(t)$, and the time constant, $\tau_h(t)$, to solve the right hand side of Eq. 2.2.8. For classic gating variables, both $\mathbf{h}_\infty(t)$ and $\tau_h(t)$ depend on V_m , and rarely, ionic concentrations, but never on other gating variables. Therefore, we calculate $\mathbf{h}_\infty(t)$ as

$$\mathbf{h}_\infty(t) = \sigma(\mathbf{W}_\infty \mathbf{x}(t) + \mathbf{b}_\infty), \quad (\text{Eq. 2.4.1})$$

where \mathbf{W}_∞ stands for the layer weights, \mathbf{b}_∞ is bias, and $\mathbf{x}(t)$ is the input to the GNN layer (the output of $\phi 1$ in Figure 1). We have chosen a sigmoid transfer function, σ , to enforce the 0 to 1 range for the gating variables and their steady-state values. Note the lack of a self-loop, i.e., \mathbf{h}_∞ does not directly

depend on \mathbf{h} . This is in contrast to the LSTM, where the equation counterpart to 2.4.1 includes an additional term $\mathbf{W}\cdot\mathbf{h}(t)$.

In contrast to \mathbf{h}_∞ , τ_h is not necessarily in the range $[0, 1]$ (in fact, it has unit of time). Recognizing that $0 < e^{-\Delta t/\tau} < 1$ for $\tau > 0$, we define the update rate as

$$\rho_h(t) = e^{-\Delta t/\tau_h(t)}. \quad (\text{Eq. 2.4.2})$$

Similar to Eq. 2.4.1,

$$\rho_h(t) = \sigma(\mathbf{W}_\tau \mathbf{x}(t) + \mathbf{b}_\tau), \quad (\text{Eq. 2.4.3})$$

for weight matrix and bias \mathbf{W}_τ and \mathbf{b}_τ . Combining Eqs. 2.4.1 and 2.4.3 with Eq. 2.2.8, we obtain the GNN update formula,

$$\mathbf{h}(t + \Delta t) = \rho_h(t)\mathbf{h}(t) + (1 - \rho_h(t))\mathbf{h}_\infty(t). \quad (\text{Eq. 2.4.4})$$

2.5 First-Pass Training

During the first-pass training, \mathcal{N} has full access to the *hidden* states and learns \mathcal{M} .

To prepare the training dataset, we start with Eq. 2.3.1 (repeated here),

$$\tilde{\mathbf{u}}' = \mathbf{f}(\mathbf{u}, t; \theta). \quad (\text{Eq. 2.5.1})$$

\mathcal{M} includes \mathbf{f} , θ , and the initial condition, $\mathbf{u}(0)$. Let \mathbf{u}_i be the solution to 2.5.1 at $t = i\Delta t$. In practice, we solve the model for a range of cycle lengths. Depending on the context, \mathbf{u}_i is either a k -element state vector or a $k \times l$ matrix of l column state vectors, where l is the number of the cycle lengths used for training.

We introduce three helper functions to select a subset of the state variables from \mathbf{u} : $O(\mathbf{u})$ extracts the observables, $H(\mathbf{u})$ lists the hidden gating variables handled by the GNN layer, and $\tilde{H}(\mathbf{u})$ lists the remaining variables processed by the LSTM layer. By definition, $H(\mathbf{u}) \cap \tilde{H}(\mathbf{u}) = \emptyset$ and $H(\mathbf{u}) \cup \tilde{H}(\mathbf{u}) = \mathbf{u}$.

The data should be presented in a sequential manner to a recurrent network. Hence, we train our model by feeding the data in $(\mathbf{u}_0, \mathbf{u}_1), (\mathbf{u}_1, \mathbf{u}_2), \dots$ order, where the first item of each ordered list is the input to \mathcal{N} and the second item is the expected output.

The observables generally do not contain enough information for the trained network to capture the model faithfully. We need to explicitly enforce the constraints encoded in \mathcal{M} by including the value of the hidden variables in the loss function.

Let \mathcal{N} be the entire network in Figure 1. It is composed of two sub-networks, \mathcal{N}_1 and \mathcal{N}_2 . We train \mathcal{N}_1 by feeding the observables, $O(\mathbf{u}_i)$, as input, and compare its output to the value of the gating variables in the next timestep. This adds a term proportional to $L_2(\mathcal{N}_1(O(\mathbf{u}_i)), H(\mathbf{u}_{i+1}))$ to the loss function, where L_2 stands for the square-error loss function.

Similarly, \mathcal{N}_2 is trained by adding a term $L_2(\mathcal{N}_2(O(\mathbf{u}_i)), \tilde{H}(\mathbf{u}_{i+1}))$ to the loss function. Note that \mathcal{N}_2 implicitly takes the output of \mathcal{N}_1 as part of its input.

The final loss function is the combination of the L_2 terms and a standard regularization term,

$$L(\mathbf{u}_i, \mathbf{u}_{i+1}) = L_2(\mathcal{N}_1(O(\mathbf{u}_i)), H(\mathbf{u}_{i+1})) + L_2(\mathcal{N}_2(O(\mathbf{u}_i)), \tilde{H}(\mathbf{u}_{i+1})) + \lambda L_2(W), \quad (\text{Eq. 2.5.2})$$

where W stands for all the weights in \mathcal{N} , and λ is a super-parameter, controlling the influence of the regularization term.

2.6 Second-Pass Retraining (Transfer Learning)

The network learns the theoretical model, \mathcal{M} , in the first-pass. For the second-pass, the goal is to fine-tune the model based on experimental recordings. Let $\mathbf{v}_i = O(\mathbf{u}_i)$ be the observables at $t = i\Delta t$. The training dataset is $\mathbf{X} = (\mathbf{v}_0, \mathbf{v}_1, \mathbf{v}_2, \dots)$.

The first-pass/second-pass training architecture is a form of *transfer learning*. We pre-train the network on an easier or more accessible dataset first and then modify it to learn the target dataset. Here, we keep \mathcal{N}_2 and ϕ_1 frozen and only retrain the GNN layer. Let $\mathcal{N}_{1,X}$ be \mathcal{N}_1 retrained on \mathbf{X} . Similarly, \mathcal{N}_X is the new network made of $\mathcal{N}_{1,X}$ and \mathcal{N}_2 , and W_X and L_X are the new versions of L and W . Since \mathcal{N}_2 is frozen, we have $\mathcal{N}_{2,X} = \mathcal{N}_2$.

We start with a standard loss function based on the input and the expected output of \mathcal{N}_X :

$$L_X(\mathbf{v}_i, \mathbf{v}_{i+1}) = L_2(\mathcal{N}_X(\mathbf{v}_i), \mathbf{v}_{i+1}) + \lambda L_2(W_X). \quad (\text{Eq. 2.6.1})$$

The problem with Eq. 2.6.1 is that \mathcal{N}_X can drift widely from \mathcal{N} , such that the resulting network may become uninterpretable. The solution is to add a term to the loss function to penalize the drift by linking the outputs of \mathcal{N}_1 and $\mathcal{N}_{X,1}$,

$$L_X(\mathbf{v}_i, \mathbf{v}_{i+1}) = L_2(\mathcal{N}_X(\mathbf{v}_i), \mathbf{v}_{i+1}) + \eta L_1(\mathcal{N}_{1,X}(\mathbf{v}_i), \mathcal{N}_1(\mathbf{v}_i)) + \lambda L_2(W_X), \quad (\text{Eq. 2.6.2})$$

where we introduce an additional super-parameter, η , which controls how much the network drifts during retraining. Finding the right value of η is critical in

getting correct and interpretable results. The L_1 norm in the η -term promotes a sparse solution, such that most gates stay the same, and only one or few of them are changed.

2.7 Neural ODE

It is possible to convert a trained or retrained GNN network into a neural ODE and solve it using standard ODE solvers. As mentioned above, the GNN network is designed as an integrator and can theoretically solve the model. However, it is akin to an explicit ODE solver (the GNN layer is based on the Rush-Larsen method, an explicit exponential ODE solver). Most ionic models are numerically stiff and need an implicit solver for stable integration. By converting the network into a formal neural-ODE, one can apply optimized implicit solvers to the resulting model.

The resulting ODE follows Eq. 2.3.4, where the neural network is stateless, and the state vector (\mathbf{u}) resides outside the network. Therefore, to convert a stateful recurrent network into a stateless neural network, we need to strip away any part of the network that depends on its internal state vectors. What remains is ϕ_1 and the trained weights in the GNN layer.

For each input \mathbf{u} , we feed $\mathbf{v} = O(\mathbf{u})$ into ϕ_1 and then calculate \mathbf{h}_∞ and ρ_h using Eqs. 2.4.1 and 2.4.3. Next, we calculate τ_h by inverting Eq. 2.4.2,

$$\tau_h = -\frac{\Delta t}{\log \rho_h}. \quad (\text{Eq. 2.7.1})$$

According to 2.2.2,

$$\mathbf{h}' = \frac{\mathbf{h}_\infty - \mathbf{h}}{\tau_h}, \quad (\text{Eq. 2.7.2})$$

where $\mathbf{h} = H(\mathbf{u})$. We can then combine \mathbf{h}' with the rest of the model ODEs to find a combined ODE/neural network, as in Eq. 2.3.4.

3 Results

We use the *ten Tusscher*, *Noble*, *Noble*, *Panfilov* human ventricular ionic model as our example (ten Tusscher from here on) [22]. The examples are coded in the Julia programming language [2] with the help of **DifferentialEquations.jl** ODE solving library [18] and **Flux.jl** neural network framework [12]. The GNN model and the examples are available from <https://github.com/shahriariravani/gnn>.

The ten Tusscher model is a moderate size ionic model with good numerical stability. This model has seventeen state variables: V_m , four ion concentrations, and twelve gates. Ten gates are classic Hodgkin-Huxley gates. These gates and the corresponding currents are:

1. Fast sodium current (I_{Na}): gates m , h , and j .
2. L-type calcium current ($I_{Ca,L}$): classic gates d and f , and atypical gate f_{Ca} .
3. Rapid delayed rectifier potassium current (I_{Kr}): x_{r1} and x_{r2} .
4. Slow delayed rectifier potassium current (I_{Ks}): x_s .
5. Inward rectifier potassium current (I_{K1}): non-state gate K_1 .
6. Transient outward potassium current (I_{to}): gates r and s .
7. The sarcoplasmic reticulum calcium-induced calcium-release current (I_{rel}): atypical gate g .

The following gates are encoded in the GNN layer: m , h , j , d , f , x_{r1} , x_{r2} , x_s , r , and s .

We integrated the ten Tusscher model for 20 seconds at cycle lengths 300 to 800 ms in 5 ms increments to generate 101 training data segments. The first half of each 20-second segment was discarded due to transient behavior. The output signal was re-sampled at 1 ms timestep. Of the 101 segments, 76 were randomly selected as the training dataset, and the other 25 were used for validation. Figure 2 shows three examples of the training signals at cycle lengths 320, 550, and 800 ms.

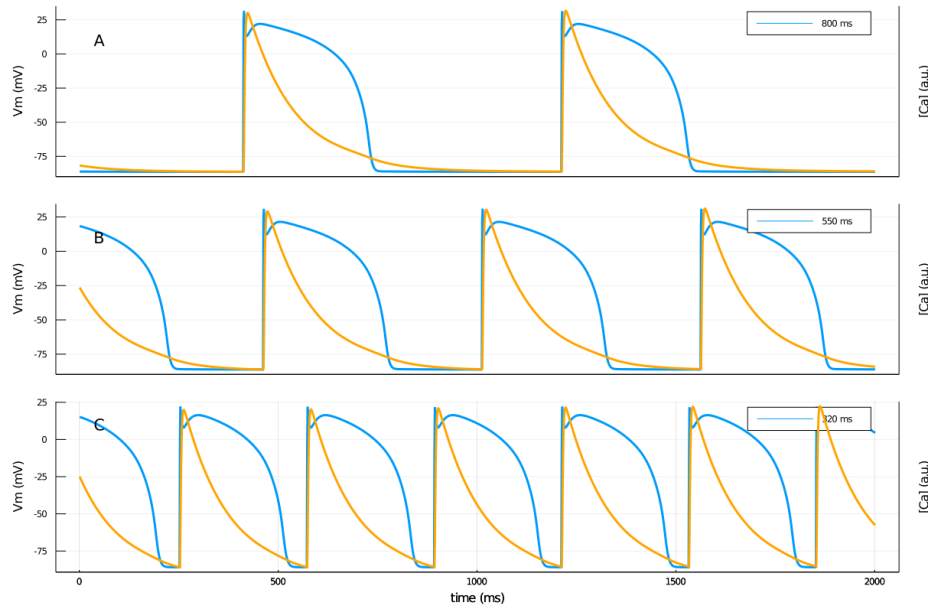


Figure 2: The observables for the ten Tusscher model at different pacing cycle lengths. The blue curve is the transmembrane potential (V_m), and the orange curve shows the intracellular calcium concentration (Ca_i).

In addition, to test the utility of the method to identify the underlying dynamics, we generated three *perturbed* datasets, corresponding to prolonged APD (**long**

qt), shortened APD (**short qt**), and increased transient outward current (**ito**) conditions (Figure 3).

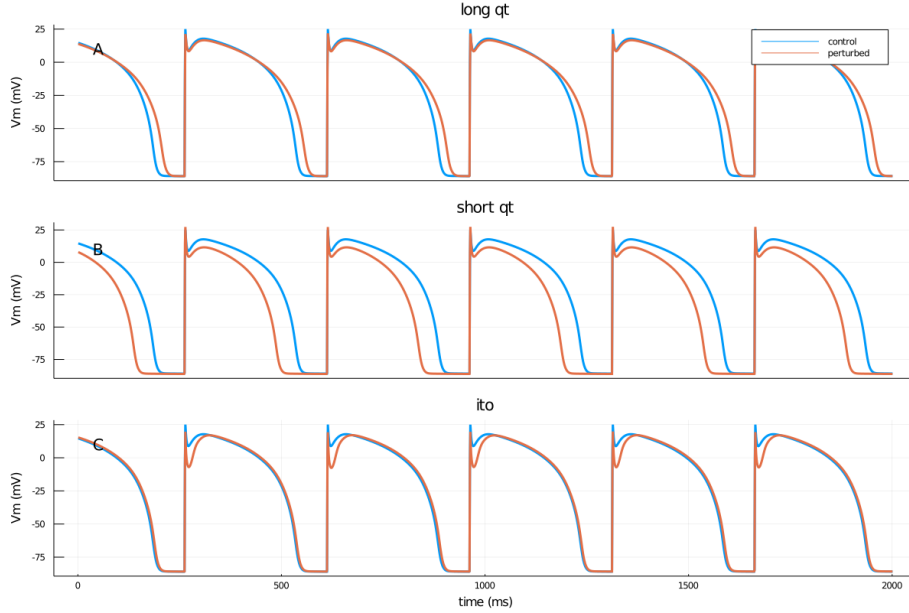


Figure 3: Transmembrane potential in different scenarios used to test the model. The blue curves are the baseline V_m . The red curves show the perturbed signals.

First-pass training of the neural network was done on the base dataset, where we assumed the network had access to the full state vector, including all the hidden variables. All the layers in ϕ_1 , ϕ_2 , and ϕ_3 had size 30. As mentioned above, the GNN layer encoded the ten classic gates. The LSTM layer was tasked with handling the remaining seven variables. A value of $\lambda = 10^{-4}$ was used for regularization.

Second-pass training was performed only on the observables: V_m and Ca_i . Considering that we didn't know the optimal value of η a priori, a range of values from 10^{-4} to 2×10^{-3} were tried.

Figure 4 depicts the base signal (blue, calculated using the standard ODE), the perturbed signal (red), and the output of the retrained network (green, using a neural ODE as in 2.7). The results suggest that the GNN network can capture the essence of the changes in the signals (e.g., APD prolongation in the long qt scenario). However, the fit between the actual signal and the output of the retrained networks is not perfect. In what follows, we discuss how the network adjusted the GNN layer weights for different scenarios.

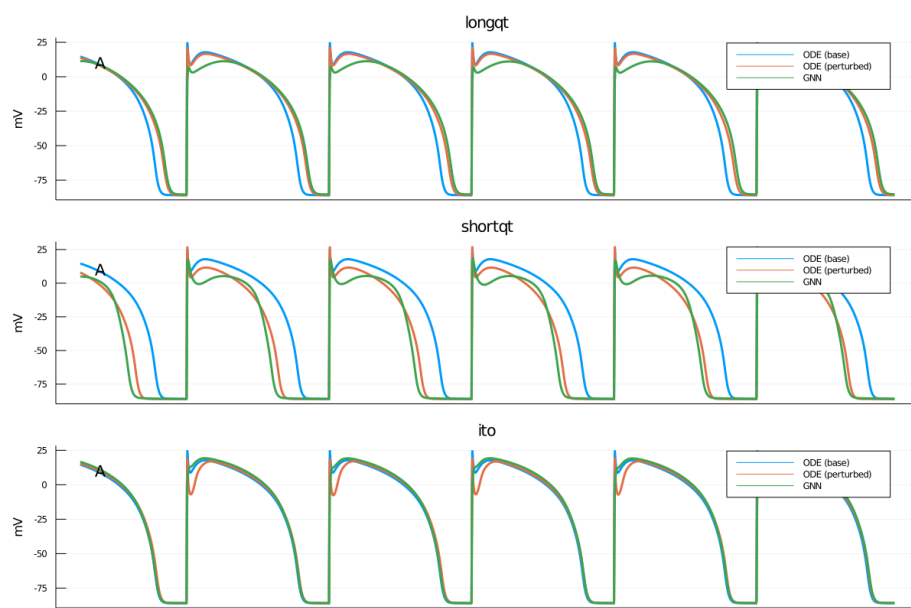


Figure 4: Comparison between the output of the neural ODE, based on the retrained GNN networks, and the output of the standard ODEs representing the models. The blue and red curves are the same as in Figure 3. The green curve is the output of the neural ODE.

3.1 Long QT

We simulated the long QT syndrome (prolonged repolarization) by reducing I_{Kr} peak conductance by 50%, while leaving the gating dynamics constant. This is a common mechanism for various medications to cause acquired long QT syndrome, which is pro-arrhythmic, potentially fatal, and of significant clinical importance.

The resulting signal is shown in Figure 3A. Figure 5 depicts ionic currents after retraining the network with the new dataset. The currents are calculated by plugging the values of the gating variables obtained from the retrained network into the corresponding equations of the ten Tusscher model. For example, to calculate the fast sodium current, we plugged m , h , j from \mathcal{N}_1 into Eq. 2.2.6.

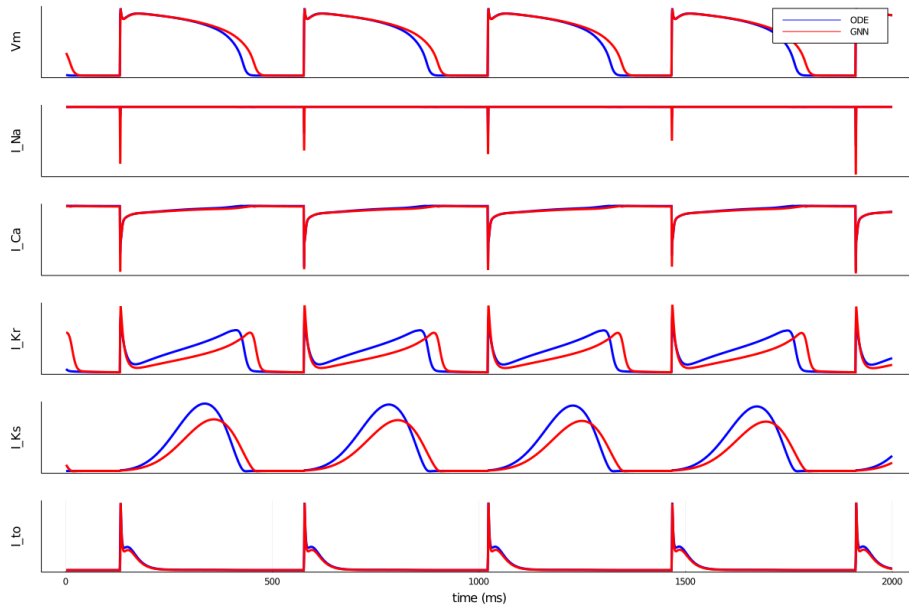


Figure 5: Comparison of the ionic currents and transmembrane potential predicted by the GNN networks retrained on the control (blue curves) and the perturbed (long qt scenario) observables (red curves). Note the reduction in both I_{Kr} and I_{Ks} currents.

The GNN network correctly deduced that reduction in potassium currents prolonged the repolarization phase. In Figure 5, both I_{Kr} and I_{Ks} are decreased; whereas, the signal was generated by decreasing only I_{Kr} . The ten Tusscher model, with 17 variables, has a large amount of redundancy. The observables alone do not contain enough information to completely constraint the model. Therefore, an exact match between the underlying mechanism of signal generation and what the network predicts is not attainable.

3.2 Short QT

The short qt scenario was generated by decreasing $I_{Ca,L}$ by 50% (Figure 3B). The retrained model currents are shown in Figure 6. The model achieved a short APD by increasing the potassium currents, which is a mechanistically valid solution. In general, the APD is determined by the balance between calcium and potassium currents during phase 2 of action potentials. Therefore, a short APD is a sign of either reduced calcium currents or increased potassium currents. Again, the observables lack enough information to break the symmetry between the two options.

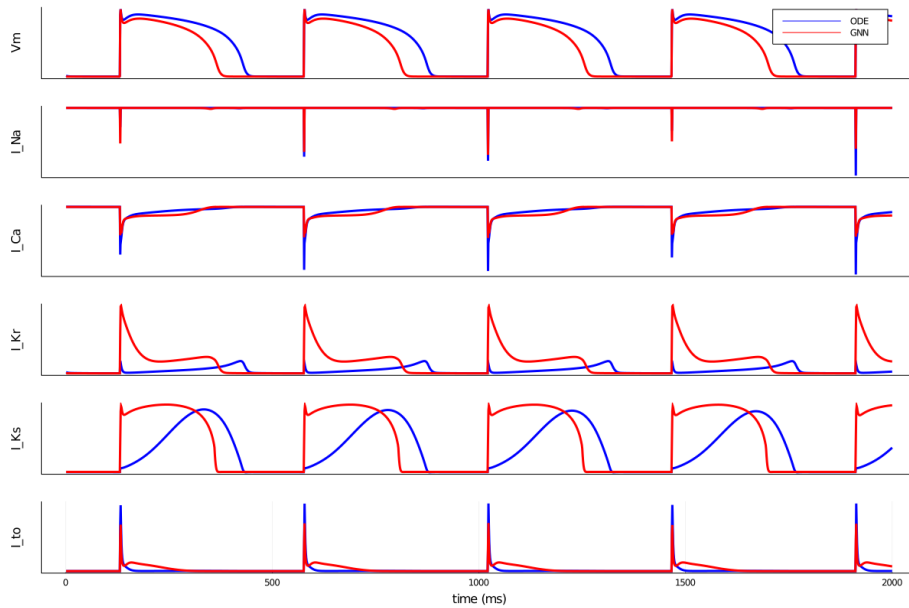


Figure 6: Comparison of the ionic currents and transmembrane potential predicted by the GNN networks retrained on the control (blue curves) and the perturbed (short qt scenario) observables (red curves). Note that both I_{K_r} and I_{K_s} currents are increased and shifted to the left.

3.3 Increased Ito

For the third scenario, we increased the I_{to} current three-fold. As a result, phase 1 of the action potential (the notch after the upstroke) became deeper. This was a difficult test for the model for two reasons. First, phase 1 is very short in duration compared to other phases of the action potential. Second, in contrast to the other two scenarios, we increased (rather than decreased) a channel conductance here. The presence of σ activation functions in Eqs. 2.4.1 and 2.4.3 prevents the model from increasing the values of any gate above 1. Moreover, the actual conductance is not part of retraining (it is implicitly

encoded in ϕ_2). One option would have been to augment the neural network by adding an affine layer after the GNN layer. However, we decided to keep the model simple and observe how it could handle the third scenario within the constraints.

The resulting currents are shown in Figure 7. The network correctly identified I_{to} as the main contributor and adjusted it accordingly. Other potassium currents were also modified to compensate for the increased current through I_{to} . Interestingly, I_{CaL} was reduced during phase 2 of action potentials to tip the balance toward potassium currents. However, we also observed undesirable changes in the calcium and, especially, sodium currents.

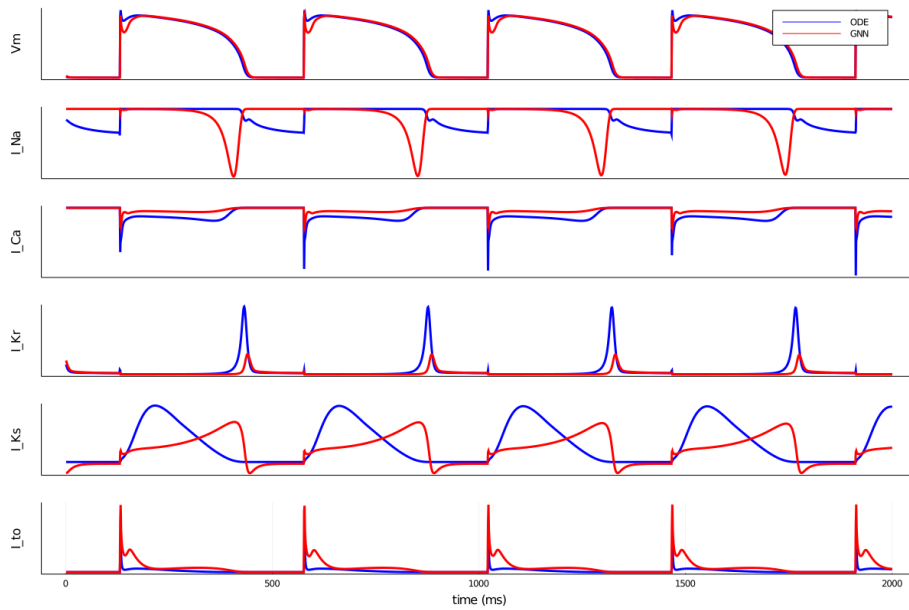


Figure 7: Comparison of the ionic currents and transmembrane potential predicted by the GNN networks retrained on the control (blue curves) and the perturbed (ito scenario) observables (red curves). Note the significant increase in the I_{to} current. Refer to the text for the discussion of other currents.

4 Discussion

In this paper, we demonstrated the feasibility of optimizing complex cardiac and neuronal ionic models trained on limited data sets (containing only observable subsets of state variables) with the help of domain-specific recurrent neural networks. We designed the network to capture the dynamics of the system. This allowed us to train the neural network to learn the theoretical model, represented by a system of ODEs, and interpret the results after the network was retrained on observables.

Historically, fine-tuning ionic models has been done either in an ad hoc fashion by manual trial and error or in a more systemic way by utilizing various optimization techniques, such as ODE sensitivity analysis and population methods [1, 3, 4, 11, 13, 16, 21]. We believe that our methods, or more generally domain-specific machine-learning methodology, augments but does not replace the traditional methodology. In traditional optimization, one selects a limited group of parameters, e.g., the peak ionic conductance, to optimize against the experimental data, whereas, when using neural networks, the parameter space is much larger and includes the general shapes of the functions describing the details of the model. Therefore, it is reasonable to use the domain-specific neural networks in the exploratory phase to determine the general shape of the functions and then apply standard optimization techniques for further fine-tuning.

We presented a motivating example in the Introduction about the sub-optimal match between an established ionic model and experimental data. As discussed in the Results section, we explored the utility of the network with a GNN layer in solving the mismatch problem. The GNN-based network was able to learn the model and morph to the observable data. We were able to interpret the network after it was retrained on the perturbed data series. The interpretations were physiologically valid but different from the way the signals were generated in the first place. The main reason for this difference is that ionic models have many parameters and are generally over-determined based on experimentally available data. Linking the control and treated networks by the η -term in Eq. 2.6.2 restricted the parameter-space. However, even the restricted space was large enough to prevent a unique solution. One way to further limit the parameter-space is to impose additional constraints on the model. For example, if we know that a given drug X is an I_{Kr} blocker, it makes sense to add a weighting-factor to the η -term to encourage the model to preferentially modify x_{r1} and x_{r2} gates.

References

- [1] Alessandro Barone, Flavio Fenton, and Alessandro Veneziani. Numerical sensitivity analysis of a variational data assimilation procedure for cardiac conductivities. *Chaos*, 27:093930, 9 2017.
- [2] Jeff Bezanson, Alan Edelman, Stefan Karpinski, and Viral B. Shah. Julia: A fresh approach to numerical computing. *SIAM Review*, 59:65–98, 1 2017.
- [3] Oliver J. Britton, Alfonso Bueno-Orovio, Karel Van Ammel, Hua Rong Lu, Rob Towart, David J. Gallacher, and Blanca Rodriguez. Experimentally calibrated population of models predicts and explains intersubject variability in cardiac cellular electrophysiology. *Proceedings of the National Academy of Sciences*, 110(23):E2098–E2105, 2013.
- [4] Darby I. Cairns, Flavio H. Fenton, and E. M. Cherry. Efficient parameterization of cardiac action potential models using a genetic algorithm. *Chaos*, 27:093922, 9 2017.

- [5] R. H. Clayton, O. Bernus, E. M. Cherry, H. Dierckx, F. H. Fenton, L. Mirabella, A. V. Panfilov, F. B. Sachse, G. Seemann, and H. Zhang. Models of cardiac tissue electrophysiology: Progress, challenges and open questions, 1 2011.
- [6] F. H Fenton and E. M. Cherry. Models of cardiac cell. *Scholarpedia*, 3(8):1868, 2008.
- [7] Felix A. Gers, Jürgen Schmidhuber, and Fred Cummins. Learning to forget: Continual prediction with lstm. *Neural Computation*, 12:2451–2471, 10 2000.
- [8] Todd J. Herron, Peter Lee, and José Jalife. Optical imaging of voltage and calcium in cardiac cells & tissues, 2 2012.
- [9] Sepp Hochreiter and Jürgen Schmidhuber. Long short-term memory. *Neural Computation*, 9:1735–1780, 11 1997.
- [10] A L HODGKIN and A F HUXLEY. A quantitative description of membrane current and its application to conduction and excitation in nerve. *The Journal of physiology*, 117:500–544, 8 1952.
- [11] M. J. Hoffman, N. S. LaVigne, S. T. Scorse, F. H. Fenton, and E. M. Cherry. Reconstructing three-dimensional reentrant cardiac electrical wave dynamics using data assimilation. *Chaos*, 26, 1 2016.
- [12] Michael Innes, Elliot Saba, Keno Fischer, Dhairya Gandhi, Marco Concetto Rudilosso, Neethu Mariya Joy, Tejan Karmali, Avik Pal, and Viral Shah. Fashionable modelling with flux. *CoRR*, abs/1811.01457, 2018.
- [13] Trine Krogh-Madsen, Eric A. Sobie, and David J. Christini. Improving cardiomyocyte model fidelity and utility via dynamic electrophysiology protocols and optimization algorithms. *Journal of Physiology*, 594:2525–2536, 5 2016.
- [14] C H Luo and Y Rudy. A dynamic model of the cardiac ventricular action potential. i. simulations of ionic currents and concentration changes. *Circulation research*, 74:1071–96, 6 1994.
- [15] Thomas O’Hara, László Virág, András Varró, and Yoram Rudy. Simulation of the undiseased human cardiac ventricular action potential: Model formulation and experimental validation. *PLoS Computational Biology*, 7:e1002061, 5 2011.
- [16] Elnaz Pouranbarani, Rodrigo Weber dos Santos, and Anders Nygren. A robust multi-objective optimization framework to capture both cellular and intercellular properties in cardiac cellular model tuning: Analyzing different regions of membrane resistance profile in parameter fitting. *PLoS ONE*, 14, 11 2019.

- [17] Christopher Rackauckas, Yingbo Ma, Julius Martensen, Collin Warner, Kirill Zubov, Rohit Supekar, Dominic Skinner, and Ali Ramadhan. Universal differential equations for scientific machine learning. *arXiv preprint arXiv:2001.04385*, 2020.
- [18] Christopher Rackauckas and Qing Nie. Differentialequations.jl—a performant and feature-rich ecosystem for solving differential equations in julia. *Journal of Open Research Software*, 5(1), 2017.
- [19] R. Roscher, B. Bohn, M. F. Duarte, and J. Garcke. Explainable machine learning for scientific insights and discoveries. *IEEE Access*, 8:42200–42216, 2020.
- [20] Stanley Rush and Hugh Larsen. A Practical Algorithm for Solving Dynamic Membrane Equations. *IEEE Transactions on Biomedical Engineering*, BME-25(4):389–392, jul 1978.
- [21] Dmitrii Smirnov, Andrey Pikunov, Roman Syunyaev, Ruslan Deviatiiarov, Oleg Gusev, Kedar Aras, Anna Gams, Aaron Koppel, and Igor R. Efimov. Genetic algorithm-based personalized models of human cardiac action potential. *PLoS ONE*, 15, 5 2020.
- [22] K. H.W.J. Ten Tusscher, D. Noble, P. J. Noble, and A. V. Panfilov. A model for human ventricular tissue. *American Journal of Physiology - Heart and Circulatory Physiology*, 286, 2004.